TEM and XRD analysis of pre-transition oxide formed on ZIRLO® cladding tube

Hoyeon Bae[1], Taeho Kim[2], Ji Hyun Kim[2], Chi Bum Bahn[1,*]
[1]*School of Mechanical Engineering, Pusan National University*
Busandaehak-ro 63beon-gil, Geumjeong-gu Busan. 609-735 - Republic of Korea
[2]*School of Mechanical and Nuclear Engineering, Ulsan National Institute of Science and Technology*
100 Banyeon-ri, Eonyang-eup, Ulju-gun, Ulsan. 689-798, Republic of Korea
[*]*Corresponding author: bahn@pusan.ac.kr*

1. Introduction

Corrosion of zirconium fuel cladding in high temperature water has limited recent efforts to prolong lifetime and reloading cycles of the fuel for enhanced plant economics. To understand corrosion mechanism of Zr alloy, a considerable literature has been devoted to micro-structural studies. In ZIRLO® samples close to kinetic transition, a large variation in the sub-oxide width at different metal/oxide interface locations are observed, and this fact suggests that the transition is an extremely local process [1]. The oxide transition has been proposed to be caused by accumulated stresses during oxide growth and interconnected porosity [2]. The metal/oxide interface roughness is linked to location of cracks [3], formation of the cracks is also associated with the transition of the oxide [3,4] and large compressive stresses caused by oxide volume expansion [5,6,7]. The cracks found in the oxide are mainly oriented parallel to the metal/oxide interface. They are more likely to work as obstacles for diffusion of oxidizing species rather than as easy diffusion paths [8]. Bossis et al. reported a porous outer layer in a pre-transition oxide by ion mass spectrometry (SIMS) and electrical impedance spectroscopy (EIS) experiments [3]. Cox et al. anticipated that porosity provides connected paths between external oxidizing medium and the underlying metal [9]. Ni et al. reported interconnected nano-pores along with grain boundaries in the oxide and concluded that development of interlinked porosity down to the metal/oxide interface is a key mechanism for the transition in oxidation kinetics [1]. Gong et al. also reported nano-pores in strings formed on Zr-Nb-Y alloy and N18 alloy (Zr-0.39Nb-0.93Sn-0.31Fe-0.08Cr-0.048O) at grain boundaries and they suggested that initiation mechanism of porosity is Kirkendall effect [10]. In the oxide, columnar grains are more dominant in inner part and equiaxed grains are frequently observed at oxide surface. It also appears that larger columnar grains have better corrosion resistance than smaller equiaxed grains [11,12,13]. Gabory et al. showed large amorphous ZrFeNb precipitates which were observed far away (700 nm) from the metal/oxide interface, while closest small amorphous β-Nb precipitates were found at 400 nm position from the metal/oxide interface in ZIRLO® samples and deduced that large ZrFeNb precipitates can stay unoxidized longer in the oxide than the smaller β-Nb precipitates [14]. In addition, lately, there is an attempt to increase dissolved hydrogen concentration to reduce crack growth rates of pressure boundary materials. Kass showed hydrogen pick up rate in Zircaloy-2, Ni-free Zircaloy-2 and Zircaloy-4 as a function of hydrogen pressure [15]. However, the effect of high concentration of hydrogen to zirconium fuel cladding has not been reported well.

We report here microscopic examination of early pre-transition (300-hour), mid pre-transition (50-day) and immediately before first transition (100-day) oxide formed on ZIRLO® cladding tube samples by using scanning transmission electron microscopy (STEM) with focused ion beam technique (FIB) and x-ray diffraction (XRD).

2. Materials and techniques

Commercial zirconium alloy, ZIRLO® tube has been oxidized in an autoclave of a recirculation loop at 360℃ and 20 MPa for 300-hour (12.5-day), 50-day and 100-day under simulating primary water chemistry conditions (pure H_2O with dissolved hydrogen of 30 cc/kg, 2 ppm Li as LiOH and 1200 ppm B as H_2BO_3). The pressure difference between interior and exterior of the cladding sample was maintained at 11.7 MPa during the exposure in the test loop in order to simulate the compressive stress condition in the actual fuel cladding. The sample information in this work is given in Tab. 1. After a corrosion test, a protective coating of platinum was deposited on the oxide surface, and then in-situ lift-out FIB sectioning was carried out on a FEI Quanta 3D FEG, instrument operated at 2-30 kV, with currents between 1 pA and 65 nA to prepare STEM thin foils.

Table. 1. ZIRLO® tube samples investigated in this work.

	Nb	Sn	O	Fe	C	N	Hf	Zr
Content (wt. %)	0.96	0.76	0.62	0.18	0.1	0.03	0.002	Bal.
Outer diameter	9.5 mm							
Inner diameter	8.3 mm							
Thickness	0.6 mm							

STEM observations were carried out on a Titan G2 at operated 300 kV. The oxygen content at the metal/oxide interface and composition of second-phase particles (SPPs) were characterized respectively by energy

dispersive x-ray spectroscopy (EDS) line profile and element mapping. Example of local region of ZrO sub-oxide can be seen in Fig. 1. XRD measurements were also obtained from bulk ZIRLO® tube sample using a Bruker D8 ADVANCE instrument to characterize crystal structures.

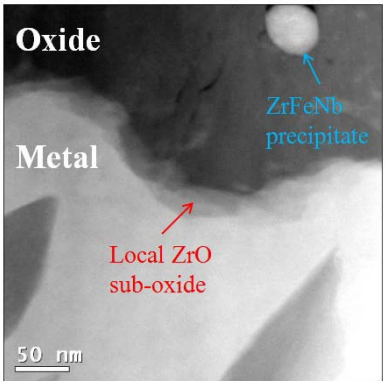

Fig. 1. Dark-field STEM image of local sub-oxide along with the metal/oxide interface.

3. Experimental Results

3.1 Oxide morphology

ZIRLO® tube samples were corroded in 360℃ autoclave of loop for 300-hour (12.5-day), 50-day and 100-day. Figure 2 shows overall oxide depending on each exposure time. Lateral cracks related to undulating metal/oxide interface can be clearly seen (red circles). These large lateral cracks are located just above the metal/oxide interface summit and have approximately 500-1000 nm length. There is possibility that the width of these cracks were extended during the FIB sectioning.

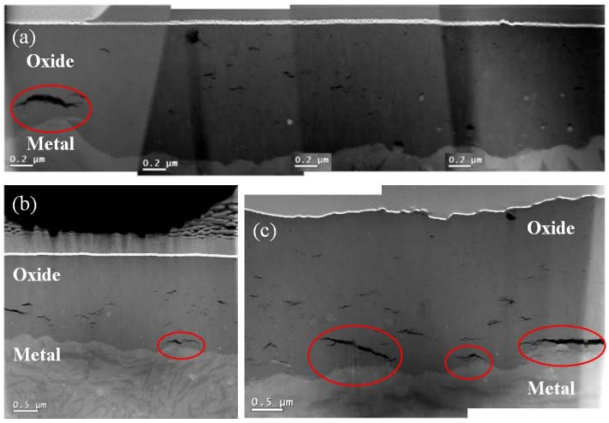

Fig. 2. (a) Dark-field STEM images showing 300-hour corroded sample oxide. (b) 50-day sample oxide. (c) 100-day sample oxide. Large cracks are related to undulating metal/oxide interface are indicated to red circles.

Detailed oxide thickness information is presented in Tab. 2. All oxide layers are composed of columnar oxide grains near the metal/oxide interface (Fig. 3(a)) and equiaxed grains are dominant in the oxide near water/oxide interface (Fig. 3(b)). Nano size voids and round shape crack are also observed in the outer oxide

Table. 2. Average thickness and standard deviation of oxide.

	Average thickness (nm)	Standard deviation (nm)
300-hour (12.5-day)	960	87.62
50-day	1860	119.81
100-day	2172	87.18

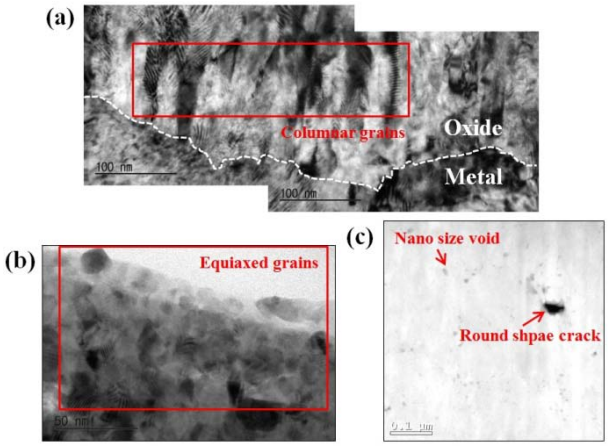

Fig. 3. (a) TEM image showing columnar grains near metal/oxide interface (300-hour corroded sample). (b) TEM image showing equiaxed grains near water/oxide interface (50-day corroded sample). (c) Dark-field STEM image showing nano size voids and round shape crack in the outer oxide (100-day corroded sample).

(Fig. 3(c)). It seems that the crack tend to have round shape in the outer oxide. Precipitates are clearly observed near the metal/oxide interface, but as getting closer to the water/oxide interface, they are gradually amorphized.

3.2 Metal/oxide interface

Local faint part along the metal/oxide interface was found. Typical this faint part can be seen in Fig. 4(a) (300-hour corroded sample) and EDS line profile of that is given in Fig. 4(b). Since the faint part has Zr : O ratio of 1 : 1 (between 45 and 55 at. %), this part is assumed as ZrO sub-oxide layer which has about 20 nm width.

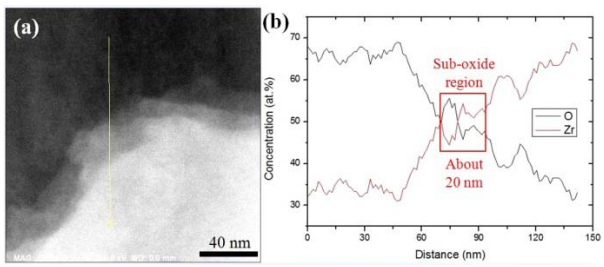

Fig. 4. (a) Dark-field STEM image of the faint part at the metal/oxide interface (300-hour corroded sample). (b) EDS line profile data of (a).

EDS line profile at the metal/oxide interface that has no sub-oxide layer is shown in Fig. 5. On the contrary, the metal/oxide interface has a sudden change of Zr : O ratio. Columnar grains are dominant near the metal/

oxide interface without porosity in all samples (300-hour, 50-day and 100-day) as shown in Fig. 3(a), and this demonstrates corrosion resistance of inner oxide formed on ZIRLO® pre-transition samples.

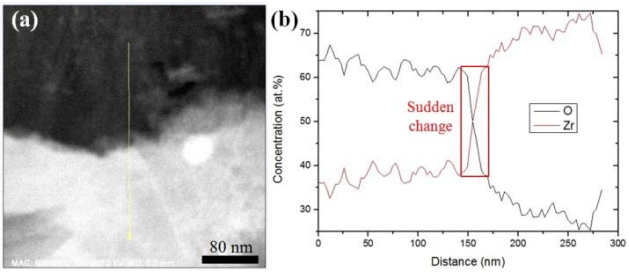

Fig. 5. (a) Dark-field STEM image of the obvious metal/oxide interface (300-hour corroded sample). (b) EDS line profile data of (a).

3.3 Water/oxide interface

Figure 6 shows dark-field STEM images of the oxide near water/oxide interface according to exposure time.

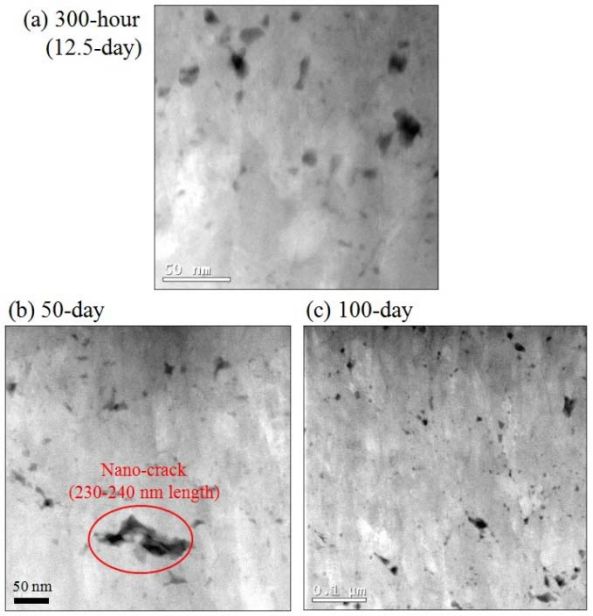

Fig. 6. (a) Dark-field STEM image of 300-hour corroded sample oxide near water/oxide interface. (b) 50-day corroded sample oxide from similar location with (a). (c) 100-day corroded sample oxide near water/oxide interface.

Nano size voids and a nano-crack which has 230-240 nm length (Fig.6(b)) are clearly seen. Successive images from the oxide near water/oxide interface to metal/oxide interface are shown in Fig. 7. As images getting closer to the metal/oxide interface, the number density of voids tends to decrease. Finally, in the image near the metal/oxide interface, voids are almost not observed. Furthermore, as exposure time increase, void-region becomes broader. But some voids might be contamination during FIB sample preparation.

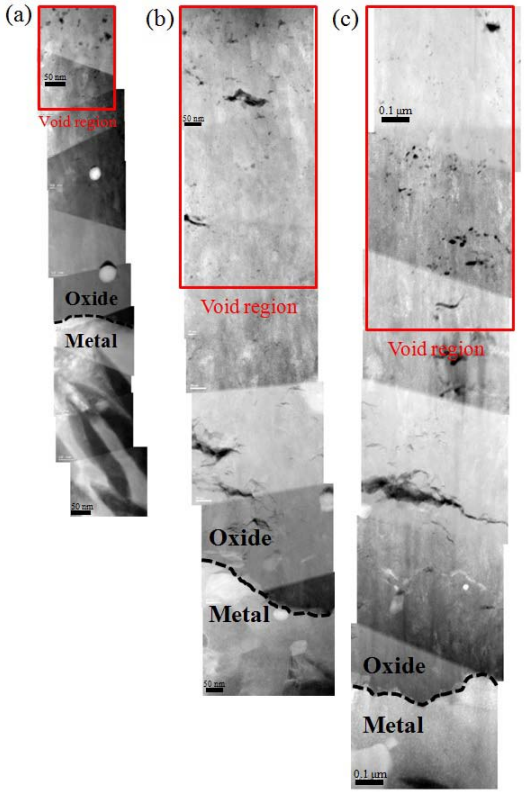

Fig. 7. (a) Dark-field STEM images of 300-hour corroded sample oxide from water/oxide interface to metal/oxide interface. (b) 50-day corroded sample oxide images which are obtained in the same way of (a). (c) 100-day corroded sample oxide.

3.4 Second-phase particles

Two types of SPPs are typically observed in ZIRLO® tube samples. Those are β-Nb precipitate and ZrFeNb precipitate. ZrFeNb precipitate is bigger than β-Nb precipitate and keeps unoxidized state longer. Fig. 8(a) and (b) show respectively smaller β-Nb precipitates and ZrFeNb precipitate near the metal/oxide interface in 300-hour corroded sample with EDS element mapping data. These precipitates have a crack on top. Figure 9 shows precipitates in 50-day corroded sample. It should

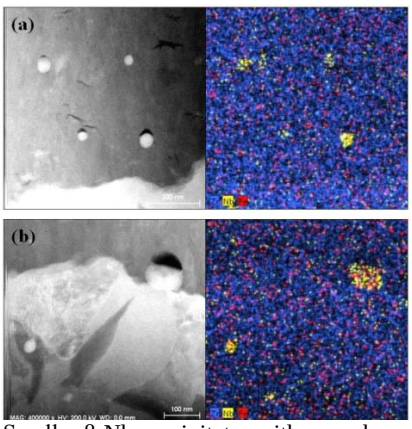

Fig. 8. (a) Smaller β-Nb precipitates with a crack on top in the oxide near metal/oxide interface. (b) Bigger ZrFeNb precipitate at the metal/oxide interface. It also has a crack on top. (a) and (b) are acquired in 300-hour corroded sample.

be noted that a crack is present on top of some precipitates (red circles) but others do not (blue circles). This also happens in 100-day corroded sample as shown in Fig. 10. Therefore, we conclude that cracks located on top of precipitate are formed during sample preparation by the FIB technique.

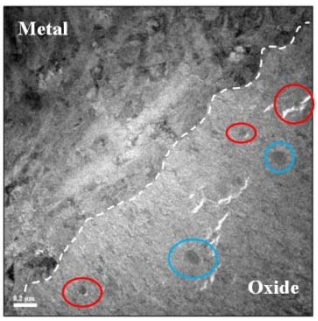

Fig. 9. Precipitates in the oxide formed on 50-day corroded sample. Some have a crack on top (red circles) but others do not (blue circles).

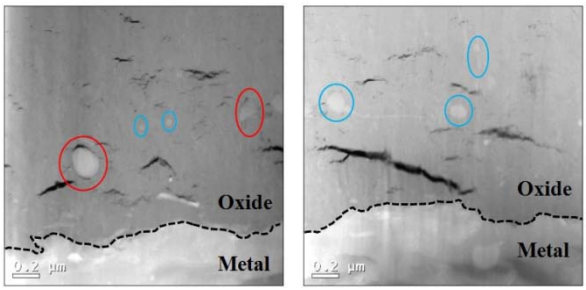

Fig. 10. Precipitates in the oxide formed on 100-day corroded sample. Some have a crack on top (red circles) but others do not (blue circles).

3.5 Hydrides

Figure 11 shows XRD peak data taken from 300-hour and 50-day corroded bulk ZIRLO® tube sample. XRD data shows a weak peak of tetragonal ZrO_2 near 30° in 2-Theta comprising the great majority of α-Zr and monoclinic ZrO_2 peaks. Peak intensities of monoclinic and tetragonal phases become stronger as sample exposure time to high temperature water increases. However, zirconium hydride peak is not detected.

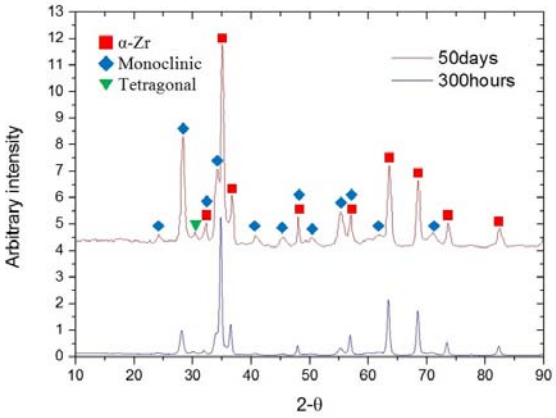

Fig. 11 XRD peak data taken from 300-hour and 50-day oxidized bulk ZIRLO® tube sample.

Therefore, hydrogen content analysis is also conducted in room temperature (23 ± 3 ℃). Results can be seen in Tab. 3. We assume that zirconium hydride may be formed too small to be detected by in-house XRD analysis up to 50-day corrosion time in 360℃. It should be noted that gas is not fed during FIB sectioning except Pt which is coating material. Thus, hydride may not be developed by sample preparation. XRD analysis and hydrogen content analysis of 100-day corroded sample will be performed in future work.

Table. 3. Results of hydrogen content analysis at room temperature (23 ± 3 ℃).

Exposure time	Hydrogen content
Initial state	1.2 ppm
300-hour	2.1 ppm
50-day	1.0 ppm

4. Discussion

By examining oxide formed on ZILRO® tube samples which are corroded in 360 ℃ autoclave of loop with PWR primary water for 300-hour, 50-day and 100-day, we report characteristic of oxide at pre-transition stage. Thickness of the pre-transition oxide layer shows good agreement with previous studies [16]. Local sub-oxide parts along the metal/oxide interface have approximately Zr : O ratio of 1 : 1 (between 45 and 55 at. %). Ni et al. showed ~ 40 nm thick stoichiometry ZrO layer containing unidentified grains at the metal/oxide interface of 100-day corroded ZIRLO® RXA (recrystallized) sample [1].

Some researchers proposed that interlinked porosity at oxide grain boundaries is a key mechanism for the transition in oxidation kinetics [1,10]. In our samples, voids are observed and the number density of them decreased from the water/oxide interface to the metal/oxide interface. Furthermore, the void region becomes broader depending on the sample exposure time. To distinguish between voids and TEM beam damage, we represent Fig. 12 showing typical TEM beam damage, which looks different from the nano-voids.

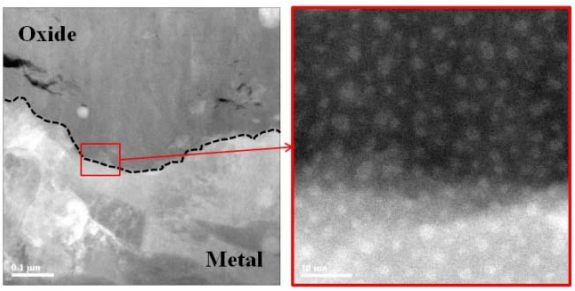

Fig. 12 Dark-field STEM image showing typical TEM beam damage at the metal/oxide interface valley region in 50-day corroded sample.

Meanwhile, Ly et al. suggested correlation between transition time and compressive hoop stress in the oxide

layer and carried out modeling based on stress [17]. Parise et al. presented the stress distribution of the undulated interface through the metal-oxide system modeling during Zr alloy oxidation as shown in Fig. 13 [18]. Very large lateral cracks are often observed in immediately above the metal/oxide interface summit.

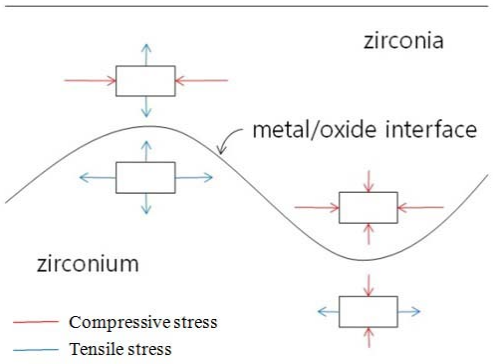

Fig. 13. Schematic stress distribution of undulated metal/oxide interface.

Also, some lateral cracks are found on top of precipitates. The cracks located on top of precipitate might be formed during the sample preparation by the FIB technique because precipitates did not always have the cracks on top. However, Tejland et al. suggested a theoretical mechanism of the crack initiation on top of the precipitates [19]. In the oxide near water/oxide interface, cracks tend to have round shape. Undulation of the metal/oxide interface causing unstable stress state is believed to generate lateral cracks near the metal/oxide interface summit, whereas the cause of formation of round shaped cracks near the outer oxide is not well known. Two types of precipitates (ZrFeNb precipitate and β-Nb precipitate) are observed, though the exact amorphization mechanism of precipitate is also not well known.

It is planned to conduct Zn injection experiments (water condition will be the same as this work except Zn injection). The pre-transition samples will be compared with samples obtained from Zn injection experiments.

5. Conclusions

TEM and XRD analysis were conducted to characterize the oxide formed on ZIRLO® cladding tube samples oxidized in an autoclave of a recirculation loop at 360 ℃ and 20 MPa for 300 hour (12.5 day), 50 day and 100 day under simulating primary water chemistry conditions. The main conclusions are as follows:

- The 300-hour, 50-day and 100-day samples have average oxide thickness of 0.96, 1.8 and 2.172 μm, respectively. Lateral cracks and columnar grains are dominant near the metal/oxide interface, while nano-voids, round shape cracks and equiaxed grains are dominant near the water/oxide interface. Very large lateral cracks are observed immediately above the metal/oxide interface summit that is least advanced. However, there is a possibility that the width of this crack was extended during the FIB sectioning.

- A local sub-oxide layer is shown as a faint part on dark-field STEM image along the metal/oxide interface, which has approximately Zr:O ratio of 1:1 (between 45 and 55 at.%).

- Voids are observed in the oxide near the water/oxide interface. As getting closer to the metal/oxide interface, the number density of voids tends to decrease. Furthermore, the void region becomes broader depending on exposure time.

- ZrFeNb precipitate and β-Nb precipitate are mainly observed. ZrFeNb precipitate is bigger than β-Nb precipitate and stays unoxidized longer. Both precipitates have a crack on top in 300-hour corroded sample. However, in 50-day and 100-day corroded samples, the crack is not necessarily present on top of precipitates.

- XRD peak data taken from bulk ZIRLO® tube samples show the great majority of α-Zr and monoclinic ZrO_2 peaks. A weak peak of tetragonal ZrO_2 is observed. Peak intensities of monoclinic and tetragonal phases become stronger as increasing the exposure time. However, zirconium hydride peak is not detected. We assume that zirconium hydride may be formed too small to be detected. It should be noted that no gas is fed during FIB sectioning except Pt which is coating material. Thus, hydride may not be developed by the sample preparation.

Acknowledgements

This work was financially supported by the International Collaborative Energy Technology R&D Program (No. 20138530030010) of the Korea Institute of Energy Technology Evaluation and Planning (KETEP).

References

[1] Ni, N., Hudson, D., Wei, J., Wang, P., Lozano-Perez, S., Smith, G. D. W., & Grovenor, C. R. M. (2012). How the crystallography and nanoscale chemistry of the metal/oxide interface develops during the aqueous oxidation of zirconium cladding alloys. Acta Materialia, 60(20), 7132-7149.
[2] A.T. Motta, M.J.G. Da Silva, A. Yilmazbayhan, R.J. Comstock, Z. Cai, B. Lai, in: 15th International Symposium on Zr in the Nuclear Industry, Sunriver, OR, United States, American Society for Testing and Materials ASTM STP 1505, 2009, pp. 486–506.
[3] Bossis, P., Lelievre, G., Barberis, P., Iltis, X., & Lefebvre, F. (2000). Multi-scale characterization of the metal-oxide interface of zirconium alloys. ASTM SPECIAL TECHNICAL PUBLICATION, 1354, 918-942.
[4] Bryner, J. S. (1979). The cyclic nature of corrosion of

Zircaloy-4 in 633 K water. Journal of nuclear materials, 82(1), 84-101.
[5] Griggs, B., Maffei, H. P., & Shannon, D. W. (1962). Multiple rate transitions in the aqueous corrosion of zircaloy. Journal of the Electrochemical Society, 109(8), 665-668.
[6] Lustman, B., & Kerze, F. (Eds.). (1955). The metallurgy of zirconium (Vol. 4). McGraw-Hill Book Company.
[7] Preuss, M., Frankel, P., Polatidis, E., Wei, J., Smith, J., Wang, C. E. F., ... & Fitzpatrick, M. (2011, August). Towards a mechanistic understanding of corrosion mechanisms in zirconium alloys. In ASTM STP1529: Zirconium in the Nuclear Industry-16th International Symposium. ASTM International.
[8] Ni, N., Lozano-Perez, S., Sykes, J. M., Smith, G. D. W., & Grovenor, C. R. M. (2011). Focussed ion beam sectioning for the 3D characterisation of cracking in oxide scales formed on commercial ZIRLO™ alloys during corrosion in high temperature pressurised water. Corrosion Science, 53(12), 4073-4083.
[9] Cox, B. (2005). Some thoughts on the mechanisms of in-reactor corrosion of zirconium alloys. Journal of Nuclear materials, 336(2), 331-368.
[10] Gong, W., Zhang, H., Wu, C., Tian, H., & Wang, X. (2013). The role of alloying elements in the initiation of nanoscale porosity in oxide films formed on zirconium alloys. Corrosion Science, 77, 391-396.
[11] Beie, H. J., Garzarolli, F., Ruhmann, H., Sell, H. J., & Mitwalsky, A. (1994). Examinations of the corrosion mechanism of zirconium alloys (No. CONF-930611--). ASTM, Philadelphia, PA (United States).
[12] Park, J. Y., Yoo, S. J., Choi, B. K., & Jeong, Y. H. (2007). Oxide microstructures of advanced Zr alloys corroded in 360 C water loop. Journal of alloys and compounds, 437(1), 274-279.
[13] Yilmazbayhan, A., Breval, E., Motta, A. T., & Comstock, R. J. (2006). Transmission electron microscopy examination of oxide layers formed on Zr alloys. Journal of Nuclear Materials, 349(3), 265-281.
[14] de Gabory, B., Motta, A. T., & Wang, K. (2015). Transmission electron microscopy characterization of Zircaloy-4 and ZIRLO™ oxide layers. Journal of Nuclear Materials, 456, 272-280.
[15] Kass, S. (1963). ASTM, STP 368. In Symposium Corrosium of Zirconium alloys.
[16] Wei, J., Frankel, P., Polatidis, E., Blat, M., Ambard, A., Comstock, R. J., & Preuss, M. (2013). The effect of Sn on autoclave corrosion performance and corrosion mechanisms in Zr–Sn–Nb alloys. Acta Materialia, 61(11), 4200-4214.
[17] Ly, A., Ambard, A., Blat-Yrieix, M., Legras, L., Frankel, P., Preuss, M., & Bréchet, Y. (2011). Understanding crack formation at the metal/oxide interface during corrosion of Zircaloy-4 using a simple mechanical Model. In in press in the Journal of ASTM International (Proceedings of the 16th International Symposium on the Zirconium in the Nuclear Industry, 2010, Chengdu, Sichuan Province, Chin (9th May 2010–13th May).
[18] Parise, M., Sicardy, O., & Cailletaud, G. (1998). Modelling of the mechanical behavior of the metal–oxide system during Zr alloy oxidation. Journal of nuclear materials, 256(1), 35-46.
[19] Tejland, P., & Andrén, H. O. (2012). Origin and effect of lateral cracks in oxide scales formed on zirconium alloys. Journal of Nuclear Materials, 430(1), 64-71.